https://doi.org/10.5194/egusphere-2025-3130
Preprint. Discussion started: 28 July 2025

Upper-air secondary pollutants downward invade to planetary boundary layer by strong turbulence at the eastern steep slope of Tibetan Plateau: results from BLMP-SCB

Suping Zhao [1, 2], Shaofeng Qi [1, 3], Jianjun He [4], Ye Yu [1, 2], Longxiang Dong [1, 2], Tong Zhang [1, 2], Guo Zhao [1, 2], Yiting Lv [1, 3]

1. Key Laboratory of Cryospheric Science and Frozen Soil Engineering, Northwest Institute of Eco-Environment and Resources, Chinese Academy of Sciences, Lanzhou 730000, China.
2. Pingliang Land Surface Process & Severe Weather Research Station, Pingliang 744015, China.
3. University of Chinese Academy of Sciences, Beijing 100049, China.
4. State Key Laboratory of Severe Weather & Key Laboratory of Atmospheric Chemistry of CMA, Chinese Academy of Meteorological Sciences, Beijing 100081, China.

Corresponding author: Suping Zhao (zhaosp@lzb.ac.cn)

https://doi.org/10.5194/egusphere-2025-3130
Preprint. Discussion started: 28 July 2025

Abstract

The comprehensive filed campaign is essential to deeply understand the interactions between aerosol and planetary boundary layer (PBL) meteorology, and implement of the relevant campaign is difficult, and thus data is scarce at the complex terrain. The first planetary boundary layer meteorology and pollution at western SiChuan Basin (BLMP-SCB) was conducted from December 2018 to January 2019. The campaign provides good chance for revealing the poorly-known the impact of PBL turbulence on profiles of air pollutants. The primary particulate matter (PM) pollutants rapidly decline with the increasing altitude, while the secondary ultraviolet PM ($UVPM_{sec}$) reduces more slowly and even shows a peak at 1.5–2.0 km above sea level. The regional and long-range transports are comparable between the primary and secondary PM pollutants during the campaign. The more uniform $UVPM_{sec}$ profiles during the nighttime are mainly modulated by thermodynamic (temperature) processes, while the secondary pollutants at PBL top downward invade into PBL by some dynamic processes, i.e., mechanical turbulence and wind shear, lending to more $UVPM_{sec}$ within PBL during the daytime. This study emphasizes the importance of turbulence and wind shear for the vertical profiles of air pollutants at complex terrain, especially at the sloped terrain. The results are helpful for understanding formation mechanism of heavy air pollution at the complex terrain, and then taking the targeted countermeasures.

Keywords: Planetary boundary layer; turbulence; air pollution; complex terrain; Tibetan Plateau

https://doi.org/10.5194/egusphere-2025-3130
Preprint. Discussion started: 28 July 2025

1 Introduction

Aerosol-planetary boundary layer (PBL) interactions are found to be one of the most important mechanisms deteriorating urban air quality near the ground surface (Li et al., 2021). The effect is largely dependent on chemical components of aerosol particles and their vertical distributions (Sun et al., 2025). Black carbon (BC) induces heating in the upper PBL, and the resulting decreased surface heat flux substantially depresses the development of PBL and consequently enhances the occurrences of extreme haze pollution episodes, and this process is defined as the dome effect of BC (Ding et al., 2016). BC can also enhance PBL development depending on the properties and altitude of the BC layer. Slater et al. (2022) applied a high-resolution model to quantify the impact of BC at different altitudes on PBL dynamics in Beijing, and found that BC within the PBL increases maximum PBL height by 0.4% but that the same loading of BC above the PBL can suppress PBL height by 6.5%. Briefly, the different optical properties of aerosol particles (absorption and scattering) at the varying altitudes exist contrasting impact on PBL dynamics, i.e., the stove, dome, and umbrella effects of aerosol particles (Ma et al., 2020).

The vertical profiles of both chemical composition and the corresponding optical properties of aerosol particles are mainly influenced by vertical mixing and regional transport (Guan et al., 2024; Tian et al., 2017). The aerosol particles within PBL are more modulated by vertical mixing of local emissions, while those above PBL are mainly affected by regional transport from upstream sources, such as biomass burning or dust (Yin et al., 2020; Zhao et al., 2019a). The biomass burning and coal combustion with the open-hearth furnace at mountaintop over Tibetan Plateau (TP) can be transported to above downstream basin due to mountain-valley breeze or mountain-plain winds induced by terrain forcing (Zhao et al., 2023). Unlike BC particles, light-absorbing efficiencies of brown carbon (BrC) were found to be significantly increased with elevation from western Sichuan Basin to eastern TP, attributing to the enhancement in secondary formation and changing sources with the increasing elevation (Qi et al., 2025; Zhao et al., 2022). Dark BrC from biomass

https://doi.org/10.5194/egusphere-2025-3130
Preprint. Discussion started: 28 July 2025

burning contributes a substantial radiative effect of +0.208 W m^{-2} (+0.02 to 0.68 W m^{-2}) via its solar radiation absorption, comparable to BC and far exceeding traditional BrC estimates (Wang et al., 2025). The strong light-absorbing aerosols over TP are transported to above basin and then deteriorates air quality within basin by aerosol-PBL feedbacks. Therefore, the long-range transport and aerosol-PBL feedback may interact rather than act as two isolated processes as traditionally thought by investigating typical regional haze events over China (Huang et al., 2020).

Compared with the regional transport, the impact of vertical mixing on air pollution is poorly understood. The vertical mixing of energy, water vapor and pollutants easily occurs around the large-scale terrain due to thermodynamic forcing. TP is considered as an important channel transporting Asian surface pollutants to the global stratosphere in response to strong "heat pump" (Bian et al., 2020; C. F. Zhao et al., 2020), which may be enhanced due to more rapid climate warming at the high-altitude regions (S. Y. Zhao et al., 2020). BC aerosols originating from South Asia can climb over Himalaya mountains to reach inland TP and accelerate glacier melting by absorbing solar radiation (Kang et al., 2019). A dust aerosol layer was found at a height of 3–4 km above the ground at the northern slopes of TP, i.e., "suspended dust" (He et al., 2024), which closely related to strong turbulence and heatwave of desert underlying surface (Liu et al., 2024; Zhang et al., 2024). The heat contribution of dust to the anomalously warm atmospheric layer over the Tarim Basin in spring and summer are 13.77% and 10.25% respectively, which seems a northward extension of TP heat source (Zhou et al., 2022). At eastern slopes of TP, the primary pollutants from Sichuan Basin can be transported to the areas with an altitude below 3.0 km (Yin et al., 2020).

Besides upward transports, TP is a global hotspot of stratospheric intrusion. The stratospheric intrusion was considered as a dominating factor of tropospheric ozone over the TP (Yang et al., 2022), especially in the areas with high surface ozone concentrations during their peak-value month (Yin et al., 2024). In the recent study of

https://doi.org/10.5194/egusphere-2025-3130
Preprint. Discussion started: 28 July 2025

Zhang et al. (2025), ozone surges within SiChuan Basin (SCB) were found to be jointly triggered by deep stratospheric intrusions and the Tibetan Plateau (TP) topographic forcing. The intruded O_3 over TP was transported into the downstream SCB by strong downdrafts along the TP's leeward slope. However, the studies are lack of in-situ observational evidence and only focus on ozone. The invasion of upper-air secondary pollutants to PBL over deep basin is less studied and the relevant mechanisms are poorly known. Therefore, we conducted the first Boundary Layer Meteorology and Pollution at SiChuan Basin (BLMP-SCB) during the winter in 2018 (Zhao et al., 2023), which provides a good opportunity for deeply understanding the downward transport of secondary air pollutants. The results are useful for understanding the change in air pollutants and then taking targeted measures.

2 Data and methods

2.1 Data from BLMP-SCB

The first field campaign of Boundary Layer Meteorology and Pollution at SiChuan Basin (BLMP-SCB) was conducted at a rural site (Sanbacun, 103°40′38″ E, 30°54′59″ N) of eastern foothills of Tibetan Plateau in winter of 2018, lasting about 40 days (Fig. 1). A tethered balloon was used to in-situ observe the vertical profiles of key PM_1 (mass and the carbonaceous components) and gaseous pollutants (CO, NO, NO_2, O_3, TVOC) and meteorological variables (temperature, RH) within PBL. The variables were observed every three-hours (02:00, 05:00, 08:00, 11:00, 14:00, 17:00, 20:00, 23:00) during the campaign, which is helpful for understanding the PBL turbulence and its impacts. A lightweight low-cost multi-pollutant sensor package, developed by Pang et al. (2021), is very portable and suitable for aerial measurements, and thus it was carried by the tethered balloon during the campaign. The system consists of electrochemical sensors measuring gaseous pollutants and an optical counter (OPC) for PM_1 with time resolution of 10 seconds. The performances of the sensors were verified by comparing with on-ground reference instruments (Pang et al., 2021), and it was substantiated to be a reliable device for aerial measurements of PM and gaseous pollutants within PBL.

https://doi.org/10.5194/egusphere-2025-3130
Preprint. Discussion started: 28 July 2025

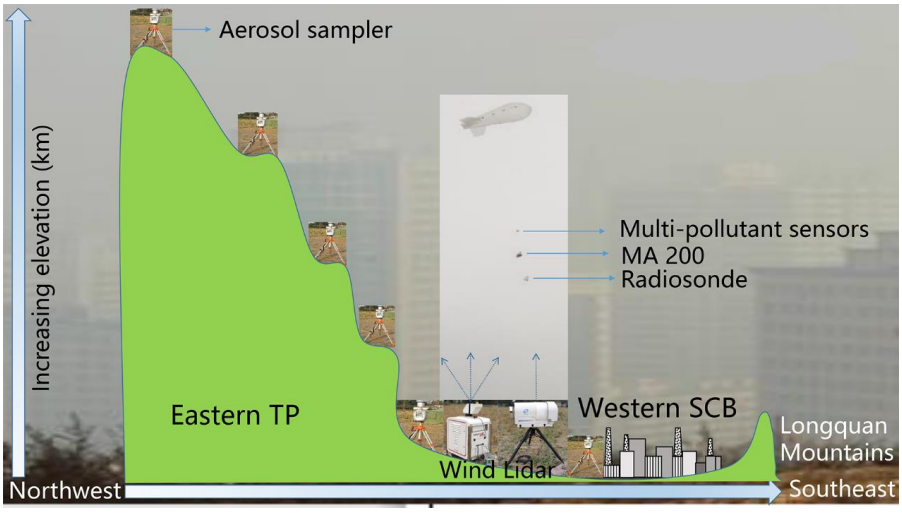

Fig. 1 Experimental set-up of 3D pollution and meteorology within PBL at the eastern foothills of Tibetan Plateau (TP).

The micorAeth MA200 (AethLabs, USA) was used to measure the mass concentrations of carbonaceous components of aerosol particles at five wavebands (375 nm, 470 nm, 528 nm, 625 nm and 880 nm). The carbonaceous particles measuring at 880 nm by the instrument were usually interpreted as Black Carbon (BC), while those at 375 nm ultraviolet band were thought to be Ultraviolet Particulate Matter (UVPM). The MA200 draws an air sample at a flow rate of 100 ml min^{-1} through a 3 mm diameter portion of the filter media. The light attenuation (ATN) in response to absorbance of particles collected on the 'Sensing' spot is measured relative to an adjacent 'Reference' portion of the filter where no particles are accumulated. The temporal resolution of 5 seconds was set to match the other observations during the campaign.

A portable GPS upper-air sounding system (IMET-3050) was deployed to monitor the vertical profiles of temperature and RH by carrying the radiosonde (IMET-1-AB) on the tethered balloon (Li et al., 2017). The radiosonde has been widely used and validated (Haman et al., 2012), and there is a very slight difference

https://doi.org/10.5194/egusphere-2025-3130
Preprint. Discussion started: 28 July 2025

with the other radiosondes such as Vaisala RS92 (Trapp et al., 2016). The radiosonde can be recycled during the campaign, which was verified by Zhao et al. (2023). The temporal resolution of temperature and RH data ranged from 1 to 3 seconds for each profile. The uncertainty of temperature and RH measurements was ±0.3 ^{o}C and ±5% given by the manufacturer. The profiles of horizontal winds (speed and direction) and vertical velocity were observed by a Doppler Wind Lidar (Windcube 200s, Leosphere, France). The Lidar emits a fixed pulse signal into the atmosphere, and the frequency of the pulse signal changes when the electromagnetic waves encounter the moving particles, and thus the obtained data quality was closely related to aerosol particles. The radial wind speed and direction can be retrieved by analyzing the frequency shift from emitted to backscattered signals. The Lidar has four scanning modes for different applications: plan position indicator (PPI), range height indicator (RHI), line-of-sight (LOS), and Doppler beam swinging (DBS) scan modes (Lundquist et al., 2017). The DBS mode was used in this campaign. The temporal resolutions of the horizontal and vertical winds are 0.2 and 0.05 Hz, and the vertical resolution of 50 m was used in this study. The wind data with signal-to-noise ratio lower than -26 dB were removed from the raw data. The data were averaged hourly to combine with the other measurements on the tethered balloon for understanding pollution-PBL interactions. The wind data measured by the Lidar were validated by comparing with the in-situ wind observations by Beijing 325-m meteorological tower, and no significant difference was found between the Lidar and sonic wind anemometer for wind speed and direction (Dai et al., 2020).

2.2 Identification of potential source regions for BC and UVPM

In regional and even the larger scales, we used HYbrid Single-Particle Lagrangian Integrated Trajectory (HYSPLIT) model to determine the origin of air masses and understand the difference of potential source regions between BC and UVPM during the campaign. The 96-h backward trajectories arriving at the three heights above ground level (100 m, 700 m and 1300 m, AGL) and initializing at the hour of day, the same as the launch of tethered balloon, was calculated with Global

https://doi.org/10.5194/egusphere-2025-3130
Preprint. Discussion started: 28 July 2025

Data Assimilation System (GDAS) data (0.25°×0.25°) from National Centers for Environmental Prediction (NCEP). Based on the trajectories, the concentration-weight trajectory (CWT) method (Hsu et al., 2003) was used to determine the potential source region of BC and UVPM. Additionally, combining BC and UVPM concentrations obtained by MA200 on the balloon with winds measured by the Lidar, the pollution roses were calculated at the heights of 100 m, 700 m and 1300 m AGL by the Openair package of Rplot software. The difference of potential source regions between BC and UVPM at regional and local scales can be more comprehensively understood by combining CWT method with pollution rose.

2.3 Cluster analysis methods

Clustering analysis was widely used in big-data analysis of environmental field (Sabaliauskas et al., 2013; Tunved et al., 2004), which has been considered to be a preferred technique for extracting some more valuable information. The K-means clustering technique splits the multi-dimensional data into pre-defined number of subgroups, and clusters are as different as possible from each other, but as homogeneous as possible within themselves, by iteratively minimizing the sum of squared Euclidean distances from each member to its cluster centroid. Clustering analysis was used to divide the UVPM profiles during the campaign into three groups with comparable vertical structure of UVPM within groups. The K-means clustering algorithm available in MATLAB© was used in this study.

2.4 Post-processing of on-line measured carbonaceous aerosols by MA200

The micorAeth MA200 may produce negative values in the lower mass concentrations and the higher temporal resolution, contributing up to 30% of the uncertainty for filter-based optical attenuation technique (Hagler et al., 2011), and thus the obtained raw data for vertical profiles must be corrected before analyzing the characteristics, especially for the in-situ observations at high-altitude. The optical noise-reduction averaging (ONA) program was used to post-process the negative values from our real-time profile measurements. The algorithm is to conduct variable

https://doi.org/10.5194/egusphere-2025-3130
Preprint. Discussion started: 28 July 2025

time-averaging of carbonaceous components measured by MA200 to reduce noise in the data. The ONA algorithm results in significant noise reductions and much more reasonable temporal changes in mass concentrations of carbonaceous particles (Cheng and Lin 2013; Park et al., 2010).

The estimation of secondary organic carbon ($UVPM_{sec}$) is important for determining the fraction of $UVPM_{sec}$ in UVPM. Initially, the $(UVPM_{sec}/BC)_{min}$ ratio was used as a proxy for the $UVPM_{pri}$ / UVPM ratio to estimate $UVPM_{sec}$ mass concentrations (Castro et al., 1999). However, many studies have found that $(UVPM/BC)_{min}$ ratio exhibits a degree of randomness in the actual observations, leading to significant errors, especially for the low BC concentrations at the high-altitude regions. To address this, Lim and Turpin (2002) have proposed sorting the UVPM/BC ratios in ascending order and replacing the $UVPM_{pri}$ /BC ratio with the average value of the top 10%–20% of the data, but it is lack of a universally applicable criterion for determining the appropriate percentile range. In view of the distinct sources between $UVPM_{sec}$ and BC, Millet et al. (2005) proposed a method estimating $UVPM_{sec}$ concentrations with the minimum correlation coefficient between UVPM and BC. This approach is to identify the UVPM /BC ratio (denoted as $(UVPM/BC)_{pri}$) at which the correlation between $UVPM_{sec}$ and BC is the weakest, and this ratio is used as the $UVPM_{pri}$ /BC ratio. Following this method, Wu and Yu (2016) developed a toolkit in Igor Pro for calculating $UVPM_{sec}$ mass concentration, significantly enhancing the accuracy of $UVPM_{sec}$ estimation, as shown in Eqs. (1) and (2).

$$UVPM_{pri} = (UVPM/BC)_{pri} \times BC, \quad (1)$$

$$UVPM_{sec} = UVPM - UVPM_{pri}. \quad (2)$$

In Eq. (1), $(UVPM/BC)_{pri}$ represents the ratio of $UVPM_{pri}$ to BC concentrations during the campaign.

2.5 Calculation of mechanical turbulence and wind shear

PBL turbulence is an important mechanism for modulating exchanges of energy, water vapor and greenhouse gases between land and atmosphere. The atmosphere is

https://doi.org/10.5194/egusphere-2025-3130
Preprint. Discussion started: 28 July 2025

heated by longwave radiation from land surface, and thus the thermal turbulence mainly reflects the impact of land on atmosphere (Sun et al., 2006). In addition, the mechanical turbulence, mostly induced by wind speed or directional shear, generally represents the influence of the atmosphere on the land due to the increased wind speed with altitude (Zhao et al., 2023). The mechanical turbulence index (V_{TKE}, unit: m s^{-1}) was calculated with the below equation:

$$V_{TKE} = \sqrt{\frac{1}{2}\left(\overline{u'^2} + \overline{v'^2} + \overline{w'^2}\right)}, \quad (3)$$

where, u', v' and w' are the fluctuations of three-dimensional components of winds (u, v and w) during the campaign. The vertical profiles of the index can be obtained by the above equation. The higher the index, the stronger the mechanical turbulence. Combination the profiles of V_{TKE} with air pollutants can be used to better understand the downward transport of air pollutants at the eastern foothills of Tibetan Plateau.

Referring to Mahrt (2017), we defined several measures of the wind shear. The wind speed shear was defined as

$$Sh \equiv |\delta V(\overline{u}, \overline{v})|, \quad (4)$$

where δV refers to differences of wind speed (V) between the adjacent measurement levels. Additionally, S_{vec} was defined as the magnitude of the vector shear based on the vertical differences of the wind-speed components

$$S_{vec} \equiv \sqrt{(\delta\overline{u})^2 + (\delta\overline{v})^2}. \quad (5)$$

The wind-directional shear can be quantified as the difference between the magnitude of the vector shear and the speed shear

$$S_{dir} \equiv S_{vec} - Sh, \quad (6)$$

where S_{dir} is expressed in m s^{-1}.

3 Results and discussion

3.1 Vertical profiles of air pollutants

The aerosol-PBL meteorology feedbacks are very sensitive to the altitude of carbonaceous components (Wang et al., 2018). In view of the increase in solar UV

https://doi.org/10.5194/egusphere-2025-3130
Preprint. Discussion started: 28 July 2025

radiation with altitude (Blumthaler et al., 1997), the slower decrease in UVPM than BC with altitude leads to more significant impact of UVPM on PBL meteorology (Zhao et al., 2023). To better reveal the mechanisms of more uniform UVPM profiles, we further separated $UVPM_{sec}$ from UVPM with Eqs. (1–2) and calculated the ratio of $UVPM_{sec}$ to UVPM (Fig. 2). As shown in Fig. 2, the primary UVPM ($UVPM_{pri}$) rapidly decreased with altitude and were mainly trapped in the regions with the altitude below 1.0 km, which was similar with BC profiles. The spikes of primary carbonaceous components ($UVPM_{pri}$ and BC) at 02:00 at the altitudes ranging from 0.8 km to ~1.0 km were jointly induced by both regional transport and low PBL height. Unlike $UVPM_{pri}$ profiles, the vertical distributions of secondary UVPM ($UVPM_{sec}$) were more uniform, and the differences among the profiles were more significant than $UVPM_{pri}$ profiles. Therefore, structure of UVPM profiles were dominated by the secondary formation. More interestingly, the peak of $UVPM_{sec}$ profiles was getting closer to the ground from 11:00 to 23:00, which may be related to regional transport of the secondary carbonaceous aerosols and then downward invasion by strong mechanical turbulence (Zhao et al., 2023), which will be discussed in details in the following sections.

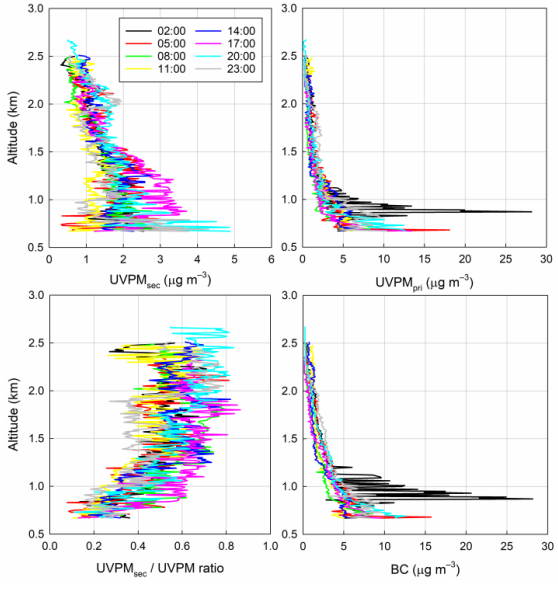

https://doi.org/10.5194/egusphere-2025-3130
Preprint. Discussion started: 28 July 2025

Fig. 2 Diurnal variations of vertical profiles of $UVPM_{sec}$, $UVPM_{pri}$, BC and $UVPM_{sec}$ / UVPM ratio during the campaign.

In order to better understand the mechanisms of the more uniform profiles of $UVPM_{sec}$ as compared to those of BC and $UVPM_{pri}$, we firstly analyzed the relationships between $UVPM_{sec}$ or $UVPM_{pri}$ and BC (Figs. 3 and S1). The $UVPM_{pri}$ concentrations linearly increased with BC at different times of the day (correlation coefficients higher than 0.99). The correlation coefficients in conjunction with coefficients of divergence (COD) are considered to better characterize the similarity of sources and the uniformity of pollutant concentrations (Wilson et al., 2005). The high correlation between BC and $UVPM_{pri}$ suggested that they shared similar sources, which does not necessarily indicate uniformity. A COD of zero means there are no differences between concentrations of the pollutants, while a value approaching one indicates maximum differences. A moderate difference is observed during the campaign on the basis of high COD values (0.108–0.179) at 02:00–11:00 and 23:00, indicating there are limited similarities between BC and $UVPM_{pri}$ at the times of the day. Specifically, the differences between BC and $UVPM_{pri}$ are getting smaller and smaller with the increasing altitudes at 02:00–11:00 and 23:00, while those are independent on altitudes with the low COD values (0.039–0.098) at 14:00–20:00 (Fig. S1). Diurnal variations of the differences between profiles of BC and $UVPM_{pri}$ are closely related to high PBL height and strong turbulent diffusion at noon and afternoon. $UVPM_{sec}$ concentrations nonlinearly varied with BC at different times of the day (Fig. 3). During the daytime, $UVPM_{sec}$ firstly increased with BC concentrations and then decreased gradually as the increased BC. The synchronous increases of $UVPM_{sec}$ and BC indicated that the low concentrations of primary emissions are favorable for secondary formation, while more primary particles inhibited secondary formation by a series of processes, such as coagulation of new particles by the large particles and scattering solar radiation. The relation of $UVPM_{sec}$ and BC is not significant during the nighttime due to the weaker secondary formation in the absence of the sun.

https://doi.org/10.5194/egusphere-2025-3130
Preprint. Discussion started: 28 July 2025

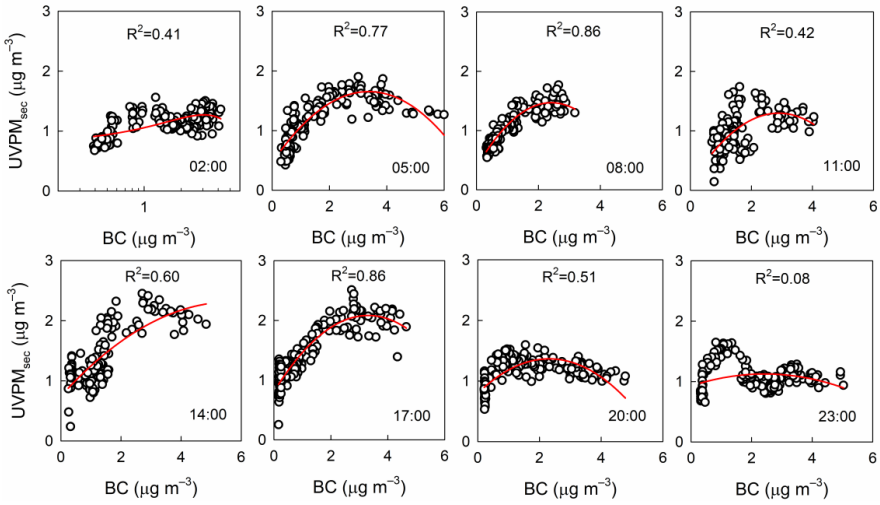

Fig. 3 Diurnal variations of the relationships between the profiles of BC and $UVPM_{pri}$ during the campaign. The relationships were fitted with the binary linear regression (red lines) and coefficients of determination (R^2) were given in each subplot.

The correlation between $UVPM_{sec}$/UVPM ratio and $UVPM_{sec}$ is weak with the coefficients of determination ranging from 0.03 to 0.38 at the whole layer (Fig. S2). Therefore, to further investigate the relationships between primary emissions and secondary formation and in consideration of planetary boundary layer (PBL) development, Fig. S3 showed the relationships between $UVPM_{sec}$/UVPM ratio and $UVPM_{pri}$ or $UVPM_{sec}$ concentrations at the varying altitude ranges at the different times of the day. Generally, the ratio increased with the strong secondary formation and decreased as the raised primary emissions. Within PBL, the primary UVPM is much higher than the secondary UVPM (the first column of Fig. S3), while the secondary formation is much stronger at the higher altitudes, resulting in the ratio significantly increased with elevation. Additionally, the relationships between $UVPM_{sec}$/UVPM ratio and $UVPM_{sec}$ are much stronger at the upper air (the coefficients of determination of 0.37 to 0.94) than those within PBL (the coefficients of determination of 0.10 to 0.67), while the correlation between the ratio and $UVPM_{pri}$ is the stronger at the low-level air. The above phenomenon also indicated that less

https://doi.org/10.5194/egusphere-2025-3130
Preprint. Discussion started: 28 July 2025

particles are helpful for the secondary formation of aerosol particles.

3.2 Impact of long-range and regional transports on aerosol vertical profiles

The long-range transport can largely impact on the vertical distributions of air pollutants, especially inside the basin terrain (Huang et al., 2008; Zhang et al., 2022). The pollutants originating from the surrounding mountain can be transported to the upper basin by multi-scale circulation, such as mountain-plain winds and valley winds, the transported pollutants impacted basin environment by aerosol-PBL feedbacks (Zhao et al., 2023). To identify the difference of impact of long-range transport on both BC and UVPM, we compared gridded back trajectory concentrations showing mean UVPM and BC concentrations using the CWT approach at 100 m, 700 m and 1300 m AGL during the campaign (Fig. 4). The gridded back trajectory concentration indicated that the high UVPM and BC concentrations at the three heights potentially originate from South Asia and central SCB. There is no significant difference for the potential source regions of BC and UVPM at each height. Therefore, the difference of vertical structures of both primary and secondary pollutants in Fig. 2 may be independent on long-range transport.

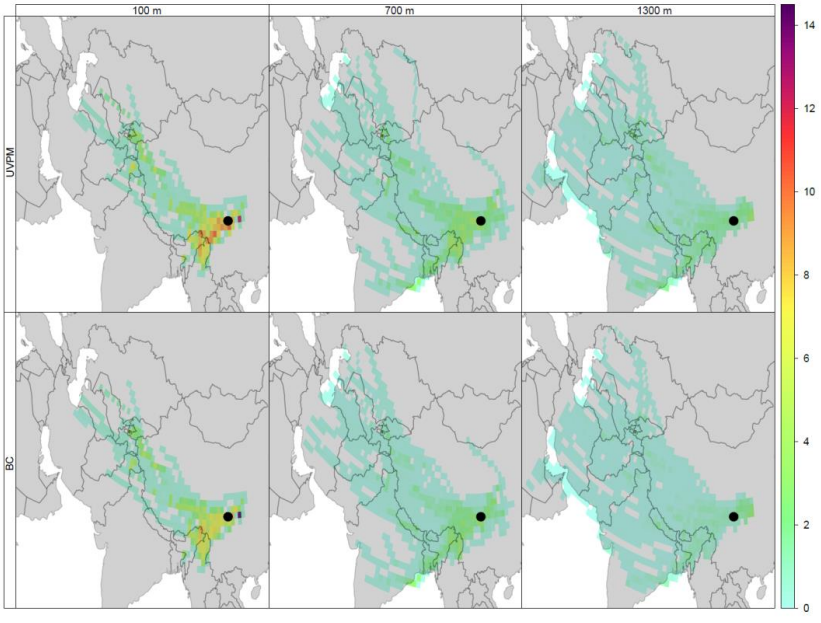

https://doi.org/10.5194/egusphere-2025-3130
Preprint. Discussion started: 28 July 2025

Fig. 4 Gridded back trajectory concentrations showing mean UVPM and BC concentrations using the CWT approach at 100 m, 700 m and 1300 m AGL during the campaign.

BC and UVPM pollution rose at the three heights also were checked to see the impact of regional transport (Fig. 5). At 100 m AGL with the highest BC and UVPM mass concentrations, the highest BC and UVPM corresponds to southwesterly and southeasterly winds. At 700 m AGL, the locations of severe BC and UVPM pollution toward the experiment site vary from southwest and south to northeast, while at the higher altitude of 1300 m AGL, the BC and UVPM origination relative to the site is mainly at northeast. Briefly, the UVPM pollution rose is consistent with BC at the three heights, and thus the regional transport is also not a key factor modulating the different vertical profiles of BC and UVPM mass concentrations during the field campaign (see Fig. 2).

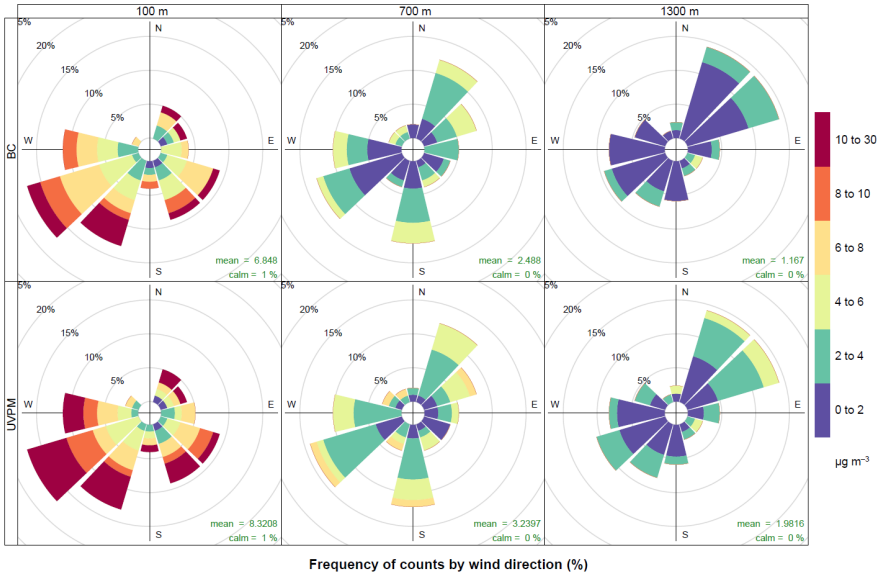

Fig. 5 BC and UVPM pollution rose at 100 m, 700 m and 1300 m AGL during the campaign. Mean BC and UVPM mass concentrations also were given in the corresponding subplot.

https://doi.org/10.5194/egusphere-2025-3130
Preprint. Discussion started: 28 July 2025

3.3 Impact of downward invasion of upper air

To extract more valuable information, the obtained $UVPM_{sec}$ profiles were divided into three groups during the campaign. The corresponding mean vertical profiles of other pollutants (BC, SO_2, O_3 and PM_1) and the meteorological factors (T, w, S_{vec}, S_{dir}, and V_{TKE}) also were calculated and showed in Fig. 6, and the frequency of each cluster at each observation hour of the day and sequence of the three clusters were showed in Fig. 7. The profile structure and magnitude of $UVPM_{sec}$ exist significant difference among the three clusters. Cluster 1, accounting for 17.28% of all profiles, mass concentrations of $UVPM_{sec}$, BC and PM_1 weakly fluctuate at the vertical direction with a weak peak of $UVPM_{sec}$ at ~ 2.0 km. Compared with Clusters 2 and 3, atmospheric stratification is more unstable in response to the much larger difference in temperature between the low-level and upper air (Fig. 6f), leading to the stronger ascending motion below 2.0 km above sea level (ASL). The vertical wind shear (S_{vec}, S_{dir}) and mechanical turbulence (V_{TKE}) are weaker as compared with that for Clusters 2 and 3, which may be mainly related to occurrence in the nighttime for Cluster 1 (Fig. 7a). O_3 concentrations were low due to weak photochemical reactions during nighttime. Therefore, the more uniform $UVPM_{sec}$ profiles during nighttime are mainly modulated by thermodynamic processes (temperature).

Cluster 2, comparable frequency of Cluster 1 (16.05%), the primary PM pollution (BC, PM_1) is the lightest, while $UVPM_{sec}$ below 1.7 km ASL (Fig. 6a) and O_3 throughout the whole layer (Fig. 6d) are the severest among the clusters. Compared with Cluster 1, $UVPM_{sec}$ concentration below 1.7 km ASL is much higher with an obvious peak around 1.4 km ASL, while above the height, it rapidly reduces to below 0.3 μg m^{-3} at ~ 2.5 km ASL, which is the lowest among the clusters. From the meteorological factor perspectives, the temperature is much lower than Cluster 1 and is comparable to Cluster 3 at the whole layer. Unlike Cluster 1, the subsiding motion is throughout the whole layer with the strongest at 2.0–2.5 ASL, and wind shear (S_{vec}, S_{dir}) and mechanical turbulence (V_{TKE}) are significantly stronger at upper air, which may be closely related to its appearance in the daytime (Fig. 7a). Therefore,

https://doi.org/10.5194/egusphere-2025-3130
Preprint. Discussion started: 28 July 2025

combining the vertical profiles of primary and secondary pollutants with meteorological factors, it is inferred that the rapid reduction in $UVPM_{sec}$ with the increasing altitude for Cluster 2 is mainly controlled by dynamic processes (wind and turbulence).

Cluster 3, accounting for two-thirds of the profiles, is the most frequent during the campaign (66.67%). The cluster appears uniformly throughout the day ranging 9% to 15%. For the cluster, secondary UVPM concentrations below 2.0 km ASL and SO_2 throughout the whole layer are the lowest among the three clusters. Similar with Cluster 2, there is weak ascending motion below 1.0 km ASL and gradually converts to subsiding motion with the increasing altitude to reach the maximum intensity at 2.0 km ASL, and the vertical structure and magnitude of mechanical turbulence index also is comparable to Cluster 2. The dynamic processes (descending motion and mechanical turbulence) are comparable between Clusters 2 and 3, but the vertical profile of $UVPM_{sec}$ is more uniform for Cluster 3 due to the relatively lower $UVPM_{sec}$ concentration at the upper air, i.e., lack of material sources. Therefore, Cluster 3 represents the background profile of $UVPM_{sec}$ at the observation site during the campaign.

As the previous mentioned, long-range and regional transports also modulate the vertical structure of air pollutants. Therefore, we checked $UVPM_{sec}$ pollution rose and gridded back trajectory concentrations showing mean UVPM and BC concentrations using the CWT approach for the three clusters during the campaign (Figs. S4 and S5). As shown in the two figures, the regional transport exists some difference among the clusters, but the highest $UVPM_{sec}$ concentrations mainly correspond to the northerly winds. For each cluster, there is small difference between UVPM and BC for the gridded back trajectory concentrations, and UVPM and BC mainly originated from South Asia and SCB. Therefore, the discrepancy among the three clusters is less influenced by regional and long-range transports, while it is more modulated by PBL meteorological processes, such as thermodynamic and dynamic processes.

https://doi.org/10.5194/egusphere-2025-3130
Preprint. Discussion started: 28 July 2025

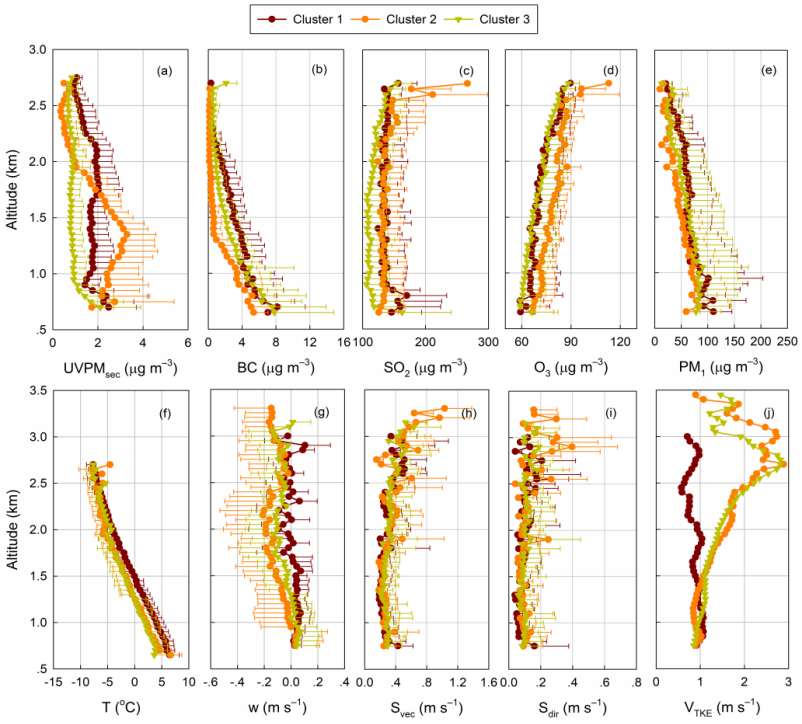

Fig. 6 (a) Three clusters of typical $UVPM_{sec}$ profiles and (b–e) the corresponding mean vertical profiles of the other air pollutants (BC, SO_2, O_3 and PM_1) and (f–j) the mean vertical profiles of temperature (T), vertical velocity (w), vector shear (S_{vec}), wind-directional shear (S_{dir}) and mechanical turbulence index (V_{TKE}) during the field campaign. The error bars showed the standard deviation among the profiles within groups at the specific height.

Based on the above analyses, we also checked the occurrence sequence of Clusters 1–3 (Figs. 7a–7d), such as the occurrence frequency of Clusters 2 and 3 at 3–21 hours with three-hours intervals after occurrence of Cluster 1 etc., which was used in the study of Zhao et al. (2021). As shown in Fig. 7a, after the occurrence of Cluster 1 (mainly appear in the nighttime), the frequency of Cluster 2 (mainly occur in the daytime) gradually increases within 3–21 hours. Therefore, it is inferred that the nighttime $UVPM_{sec}$ above 1.7 km ASL downward invades to PBL to induce the significant $UVPM_{sec}$ peak in the daytime with the development of mechanical

https://doi.org/10.5194/egusphere-2025-3130
Preprint. Discussion started: 28 July 2025

turbulence and wind shear. Zhao et al. (2023) also found that mechanical turbulence largely modulates the vertical profiles of air pollutants, which can confirm our findings. After Cluster 2, Cluster 1 is more frequent (Fig. 7c), and thus daytime $UVPM_{sec}$ within the PBL is gradually dispersed to the upper air by thermodynamic processes. Clusters 1 and 2 appear alternately during the campaign. After Cluster 3, the frequency of Clusters 1 and 2 is comparable, and the occurrence of which cluster is dependent on daytime or nighttime.

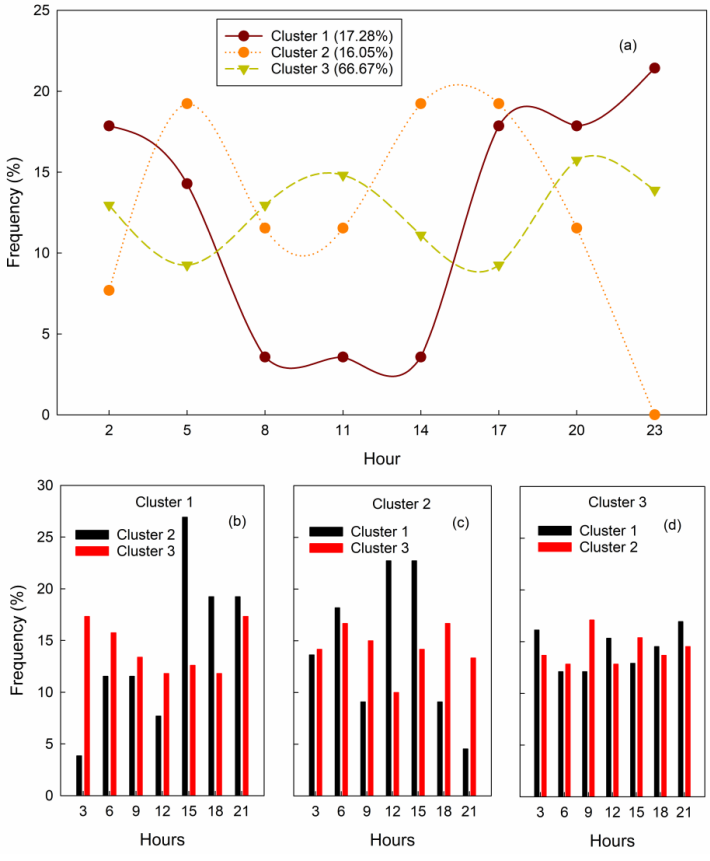

Fig. 7 (a) Diurnal variations of occurrence frequence of the three clusters of vertical profile and (b–d) occurrence frequency of the other two clusters at 3–21 hours with three-hours intervals after occurrence of the specific cluster.

We selected two typical cases on 1 and 7 January 2019 (Figs. 8 and S6) to better

https://doi.org/10.5194/egusphere-2025-3130
Preprint. Discussion started: 28 July 2025

explain the impact of thermodynamic and dynamic processes on the vertical distribution of air pollutants. On 7 January 2019, compared with rapid reduction in BC and PM_1 concentrations with the increasing altitude, $UVPM_{sec}$ concentrations change much weaker at the vertical direction with two obvious peaks near the ground surface and at 2.0–2.5 km ASL, and the location of peak varies with the time of day. From the thermodynamic processes (temperature) perspectives, the surface temperature inversion has a certain impact on the peak of air pollutants near the ground surface. However, the temperature is comparable at the upper air among the hours of the day, and thus which factors modulate the upper peak should be deeply studied. Unlike temperature profiles, the profiles of vertical velocity and wind shear (Sh, S_{vec} and S_{dir}) exist large difference among the times of the day. Furthermore, the $UVPM_{sec}$ peaks well correspond to the strong descending motion and wind shear, and thus the $UVPM_{sec}$ peaks at the upper air on 7 January 2019 are mainly modulated by dynamic processes instead of thermodynamic processes.

Similar with the previous case, the much rapider reduction of BC than $UVPM_{sec}$ with the increasing altitude on 1 January 2019. However, structure of PM_1 profiles is dominated by $UVPM_{sec}$ rather than BC. In the early morning and late evening, air pollutants are trapped below 1.0 km ASL due to the impact of temperature inversion near the ground surface induced by radiative cooling (Figs. S6a–e). As the surface is heated up and PBL developed during the daytime, the peaks of $UVPM_{sec}$ and PM_1 mass concentrations gradually get farther and farther away from the ground, and PM_1 peak reaches 2.3 km ASL at 17:00. Thereafter, location of the peak rapidly lowers and the magnitude increases significantly at 20:00. From the perspectives of vertical velocity and wind shears, the subsiding motion is significant above 1.5 km ASL throughout the day, while the ascending motion is obvious below 1.5 km ASL at 17:00. Furthermore, the wind shears (Sh, S_{vec}, and S_{dir}) are stronger above 1.5 km ASL at the daytime (11:00–17:00). Therefore, the variations of $UVPM_{sec}$ and PM_1 peaks at 1.5–2.0 km above ASL are jointly by both thermodynamic processes from the ground surface and dynamic processes from the upper air (Zhao et al., 2023), while the peaks

https://doi.org/10.5194/egusphere-2025-3130
Preprint. Discussion started: 28 July 2025

near the ground surface are mainly modulated by thermodynamic processes. Zhao et al. (2023) also found that vertical structure of UVPM and BC is largely different within SiChuan Basin, and thermodynamic and dynamic processes were used to explain the phenomenon, which can better support our findings.

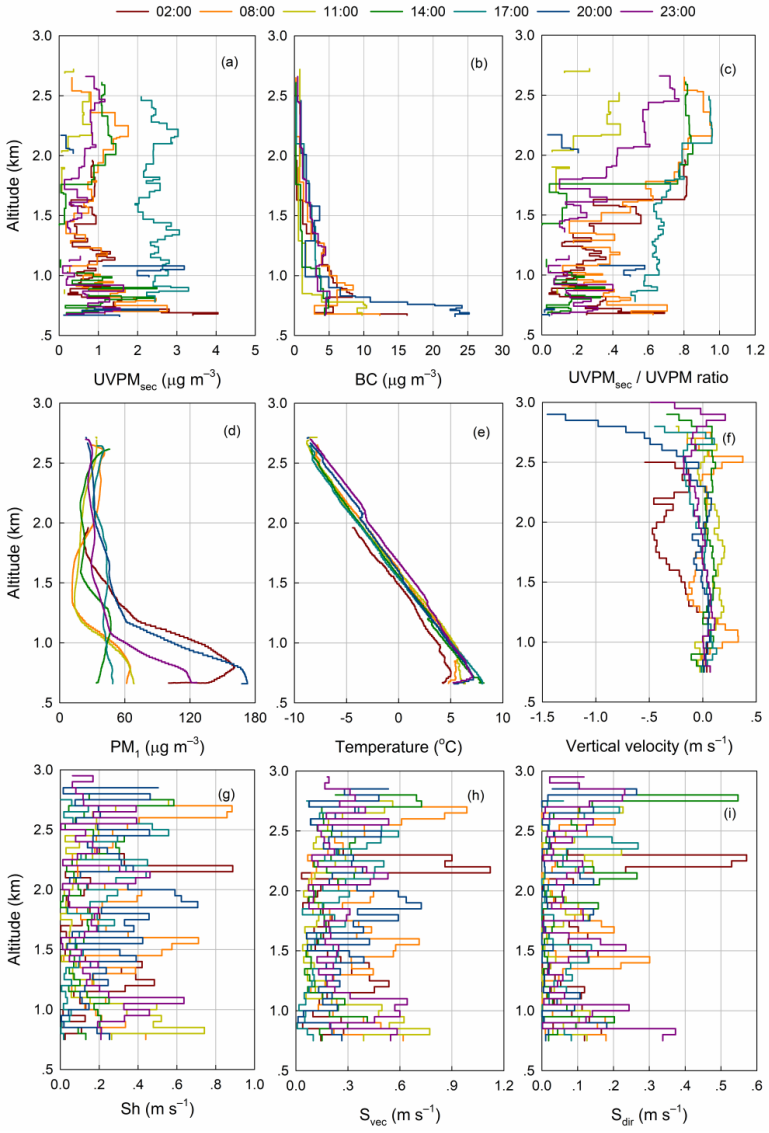

Fig. 8 Diurnal variations of air pollutants (UVPM$_{sec}$, BC, UVPM$_{sec}$/UVPM ratio, and PM$_1$) and meteorological factors (temperature, vertical velocity, Sh, S_{vec}, and S_{dir}) on 7 January 2019.

https://doi.org/10.5194/egusphere-2025-3130
Preprint. Discussion started: 28 July 2025

4 Conclusions

The first Boundary-Layer Meteorology and Pollution at SiChuan Basin (BLMP-SCB) was conducted from December 2018 to January 2019 to deeply understand the interactions between meteorology and pollution at the complex terrain. The vertical profiles of temperature, RH and air pollutants (CO, NO, NO_2, O_3, TVOC, BC, UVPM) were observed every three-hours by the instruments carried by tethered balloon. A Doppler Wind Lidar (Windcube 200s, Leosphere, France) was used to obtain the profiles of winds (wind speed and direction, vertical velocity). Based on the data from BLMP-SCB, this study analyzed the impact of mechanical turbulence and wind shear on vertical profiles of air pollutants. Some novel findings were obtained as follows.

The primary PM (BC, $UVPM_{pri}$) concentrations reduce rapidly with the altitude, while the reduction of secondary PM ($UVPM_{sec}$) concentrations is the slower and even occurs high values at 1.5–2.0 km ASL, which is explained from the two perspectives of regional transport and downward invasion of upper air in this study. There is small difference for the backward trajectories and pollution rose between BC and UVPM, and thus the discrepancy of vertical structure between BC and UVPM cannot be attributed to regional transport. Combining the clustering analysis technique with case study, the thermodynamic processes (temperature) are found to be dominant factors for the nighttime uniform UVPM profiles. However, at the daytime, the secondary air pollutants at upper PBL can downward invade into PBL by the strong dynamic processes (mechanical turbulence and wind shear), resulting in highly secondary pollutants at 1.5 km above sea level. The study is significant for deeply understanding the formation mechanism of unique profile of air pollutants and expanding the interactions between meteorology and pollution at the complex terrain.

We obtained some novel findings, while there are some limitations for this study. The field campaign of BLMP-SCB was conducted at only a rural site of eastern foothills of Tibetan Plateau, and the observation period was too short to obtain more solid

https://doi.org/10.5194/egusphere-2025-3130
Preprint. Discussion started: 28 July 2025

conclusions. Therefore, we will conduct the second Boundary-Layer Meteorology and Pollution at SiChuan Basin (BLMP-SCB II) at a rural site of Yaan City, more southern than the site of the previous campaign. Combining the data from the two filed campaigns, we hope to get some more universal laws for the interactions between meteorology and pollution at the complex terrain, especially at the sloped terrain from the basin to Tibetan Plateau. The universal conclusions are important for understanding the formation mechanism of heavy air pollution and then specifying the corresponding countermeasures.

Code/Data availability

The code and data used in this work can be accessed by contacting the corresponding author.

Author contribution

Suping Zhao and Ye Yu designed the field experiments and Tong Zhang, Guo Zhao and Shaofeng Qi carried them out. Jianjun He instructed the works. Longxiang Dong and Yiting Lv analyzed the relevant data. Suping Zhao prepared the manuscript with contributions from all co-authors.

Acknowledgements

This work was supported by the National Natural Science Foundation of China (42422504), Major Science and Technology Project of Gansu Province (24ZD13FA003), and Excellent Member of Youth Innovation Promotion Association, Chinese Academy of Sciences (Y2021111), and Youth United Funding of Lanzhou Branch of Chinese Academy of Sciences.

References

Bian J.C., Li D., Bai Z., Li Q., Lyu D.R., Zhou X.J., 2020. Transport of Asian surface pollutants to the global stratosphere from the Tibetan Plateau region during the Asian summer monsoon. *National Science Review*, 7(3), 516–533, DOI:

https://doi.org/10.5194/egusphere-2025-3130
Preprint. Discussion started: 28 July 2025

10.1093/nsr/nwaa005.

Blumthaler M., Ambach W., Ellinger R., 1997. Increase in solar UV radiation with altitude. *Journal of Photochemistry and Photobiology B-Biology*, 39(2), 130–134, DOI: 10.1016/S1011-1344(96)00018-8.

Castro L.M., Pio C.A., Harrison R.M., Smith D.J.T., 1999. Carbonaceous aerosol in urban and rural European atmospheres: estimation of secondary organic carbon concentrations. *Atmospheric Environment*, 33(17), 2771–2781, DOI: 10.1016/S1352-2310(98)00331-8.

Cheng Y.H., Lin M.H., 2013. Real-time performance of the microAeth® AE51 and the effects of aerosol loading on its measurement results at a traffic site. *Aerosol and Air Quality Research*, 13(6), 853–1863.

Dai L.D., Coauthors, 2020. Multilevel validation of Doppler Wind Lidar by the 325 m meteorological tower in the planetary boundary layer of Beijing. *Atmosphere*, 11, 1051, doi:10.3390/atmos11101051.

Ding A.J., Huang X., Nie W., Sun J.N., Kerminen V.-M., Petaja T., Su H., Cheng Y.F., Yang X.Q., Wang M.H., Chi X.G., Wang J.P., Virkkula A., Guo W.D., Yuan J., Wang S.Y., Zhang R.J., Wu Y.F., Song Y., Zhu T., Zilitinkevich S., Kulmala M., Fu C.B., 2016. Enhanced haze pollution by black carbon in megacities in China. *Geophysical Research Letters*, 43(6), 2873–2879, DOI: 10.1002/2016GL067745.

Guan X., Tian P., Wang W., Zhang M., Song X., Zhang Z.D., Zhang L., 2024. More accurate quantification of direct aerosol radiative effects using vertical profiles of single-scattering albedo derived from tethered balloon observations. *Journal of Geophysical Research-Atmospheres*, 129(14), e2023JD040605, DOI: 10.1029/2023JD040605.

Hagler G.S., Yelverton T.L., Vedantham R., Hansen A.D., Turner J.R., 2011. Post-processing method to reduce noise while preserving high time resolution in Aethalometer real-time black carbon data. *Aerosol and Air Quality Research*, 11, 539–546.

Haman C.L., Lefer B., Morris G.A., 2012. Seasonal variability in the diurnal evolution of the boundary layer in a near-coastal urban environment. *Journal of*

https://doi.org/10.5194/egusphere-2025-3130
Preprint. Discussion started: 28 July 2025

Atmospheric and Oceanic Technology, 29(5), 697–710.

He Q., Li J.L., Zhao T.L., Zhang H.L., Meng L., 2024. Observing a dust aerosol layer at a height of 3-4 km above the ground on the southern margin of the Tarim Basin. *Atmospheric Environment*, 318, 120236, DOI: 10.1016/j.atmosenv.2023.120236.

Hsu Y.K., Holsen T.M., Hopke P.K., 2003. Comparison of hybrid receptor models to locate PCB sources in Chicago. *Atmospheric Environment*, 37, 545–562.

Huang J.P., Minnis P., Chen B., Huang Z.W., Liu Z., Zhao Q., Yi Y., Ayers J.K., 2008. Long-range transport and vertical structure of Asian dust from CALIPSO and surface measurements during PACDEX. Journal of Geophysical Research-Atmospheres, 113(D23), D23212, DOI: 10.1029/2008JD010620.

Huang X., Ding A.J., Wang Z.L., Ding K., Gao J., Chai F.H., Fu C.B., 2020. Amplified transboundary transport of haze by aerosol-boundary layer interaction in China. *Nature Geoscience*, 13(6), 428–434, DOI: 10.1038/s41561-020-0583-4.

Li Z., Lyu S.H., Wen L., Zhao L., Ao Y., Wang S.Y., 2017. Effect of a cold, dry air incursion on atmospheric boundary layer processes over a high-altitude lake in the Tibetan Plateau. *Atmospheric Research*, 185, 32–43.

Lim H.J., Turpin B.J., 2002. Origins of primary and secondary organic aerosol in Atlanta: results of time-resolved measurements during the Atlanta supersite experiment. *Environmental Science and Technology*, 36(21), 4489–4496, DOI: 10.1021/es0206487.

Lundquist J.K., Coauthors, 2017. Assessing state-of-the-art capabilities for probing the atmospheric boundary layer: the XPIA field campaign. *Bulletin of the American Meteorological Society*, 2, 98.

Mahrt L., 2017. Directional shear in the nocturnal atmospheric surface layer. Boundary-Layer Meteorology, 165, 1–7, DOI: 10.1007/s10546-017-0270-1.

Millet D.B., Donahue N.M., Pandis S.N., Polidori A., Stanier C.O., Turpin B.J., Goldstein A.H., 2005. Atmospheric volatile organic compound measurements during the Pittsburgh Air Quality Study: Results, interpretation, and quantification of primary and secondary contributions. *Journal of Geophysical Research-Atmospheres*, 110(D7), D07S07, DOI: 10.1029/2004JD004601.

https://doi.org/10.5194/egusphere-2025-3130
Preprint. Discussion started: 28 July 2025

Kang S.C., Zhang Q., Qian Y., Ji Z., Li C., Cong Z., Zhang Y., Guo J., Du W., Huang J., You Q., Panday A., Rupakheti M., Chen D.L., Gustafsson Ö., Thiemens M.H., Qin D.H., 2019. Linking atmospheric pollution to cryospheric change in the Third Pole region: current progress and future prospects. *National Science Review*, 6 (4), 796–809, DOI: 10.1093/nsr/nwz031.

Li Q.H., Zhang H.S., Cai X.H., Song Y., Zhu T., 2021. The impacts of the atmospheric boundary layer on regional haze in North China. *npj Climate and Atmospheric Science*, 4(1), 9, DOI: 10.1038/s41612-021-00165-y.

Liu Y.Z., Huang J.P., Tan Z.Y., Zhou C.L., Li D., Xie Y.K., 2024. Compound events of heatwave and dust storm in the Taklamakan Desert. *Science China-Earth Sciences*, 67(7), 2073–2083, DOI: 10.1007/s11430-023-1355-1.

Ma Y., Ye J., Xin J., Zhang W., Vilà-Guerau de Arellano J., Wang S.G., Zhao D., Dai L., Ma Y., Wu X., Xia X.A., Tang G., Wang Y.S., Shen P., Lei Y., Martin S.T., 2020. The stove, dome, and umbrella effects of atmospheric aerosol on the development of the planetary boundary layer in hazy regions. *Geophysical Research Letters*, 47, e2020GL087373, https://doi.org/10.1029/2020GL087373.

Pang X.B., Chen L., Shi K., Wu F., Chen J., Fang S., Wang J., Xu M., 2021. A lightweight low-cost and multipollutant sensor package for aerial observations of air pollutants in atmospheric boundary layer. *Science of the Total Environment*, 764, 142828.

Park S.S., Hansen A.D.A., Cho S.Y., 2010. Measurement of real time black carbon for investigating spot loading effects of Aethalometer data. *Atmospheric Environment*, 44, 1449–1455.

Qi S.F., Zhao S.P., Yu Y., Kang S.C., 2025. Optical properties of carbonaceous aerosols and source impacts in the Lanzhou valley: In-situ observations by means of topographical relief. *Urban Climate*, 59, 102302, DOI: 10.1016/j.uclim.2025.102302.

Sabaliauskas K., Jeong C.-H., Yao X., Jun Y.-S., Evans G., 2013. Cluster analysis of roadside ultrafine particle size distributions. *Atmospheric Environment*, 70, 64–74.

Slater J., Coe H., McFiggans G., Tonttila J., Romakkaniemi S., 2022. The effect of BC on aerosol–boundary layer feedback: potential implications for urban pollution

https://doi.org/10.5194/egusphere-2025-3130
Preprint. Discussion started: 28 July 2025

episodes. *Atmospheric Chemistry and Physics*, 22, 2937–2953.

Sun C., Zhou Q., Xia K.Q., 2006. Cascades of velocity and temperature fluctuations in buoyancy-driven thermal turbulence. *Physical Review Letters*, 97(14), 144504, DOI: 10.1103/PhysRevLett.97.144504.

Sun P., Wang J.P., Liu Y.L., Nie W., Chi X.G., Xu Z., Ge D.F., Ren C.H., Zhu C.J., Huang X., Ding A.G., 2025. Enhanced particulate nitrate formation in residual layer exacerbates near-surface pollution: Insights from tethered airship and long-term ground measurements. *Journal of Geophysical Research-Atmospheres*, 130(4), e2024JD042672, DOI: 10.1029/2024JD042672.

Tian P.F., Cao X., Zhang L., Sun N.X., Sun L., Logan T., Shi J., Wang Y., Ji Y., Lin Y., Huang Z.W., Zhou T., Shi Y.Y., Zhang R.Y., 2017. Aerosol vertical distribution and optical properties over China from long-term satellite and ground-based remote sensing. *Atmospheric Chemistry and Physics*, 17(4), 2509–2523, DOI: 10.5194/acp-17-2509-2017.

Trapp R.J., Stensrud D.J., Coniglio M.C., Schumacher R.S., Baldwin M.E., Waugh S., Conlee D.T., 2016. Mobile radiosonde deployments during the mesoscale predictability experiment (MPEX): rapid and adaptive sampling of upscale convective feedbacks. *Bulletin of the American Meteorological Society*, 97(3), 329–336.

Tunved P., Strom J., Hansson H.-C., 2004. An investigation of processes controlling the evolution of the boundary layer aerosol size distribution properties at the Swedish background station aspvreten. *Atmospheric Chemistry and Physics*, 4, 2581–2592.

Wang Z.L., Huang X., Ding A.J., 2018. Dome effect of black carbon and its key influencing factors: a one-dimensional modelling study. *Atmospheric Chemistry and Physics*, 18(4), 2821-2834, DOI: 10.5194/acp-18-2821-2018.

Wang X., Chakrabarty R.K., Schwarz J.P., Murphy S.M., Levin E.J.T., Howell S.G., Guo H.Y., Campuzano-Jost P., Jimenez J.L., 2025. Dark brown carbon from biomass burning contributes to significant global-scale positive forcing. *One Earth*, 8(3), 101205, DOI: 10.1016/j.oneear.2025.101205.

Wilson J.G., Kingham S., Pearce J., Sturman A.P., 2005. A review of intraurban variations in particulate air pollution: implications for epidemiological research.

https://doi.org/10.5194/egusphere-2025-3130
Preprint. Discussion started: 28 July 2025

Atmospheric Environment, 39, 6444–6462, DOI: 10.1016/j.atmosenv.2005.07.030.

Wu C., Yu J.Z., 2016. Determination of primary combustion source organic carbon-to-elemental carbon (OCaEuro-/aEuro-EC) ratio using ambient OC and EC measurements: secondary OC-EC correlation minimization method. *Atmospheric Chemistry and Physics*, 16(8), 5453–5465, DOI: 10.5194/acp-16-5453-2016.

Yang J.H., Wang K., Lin M., Yin X.F., Kang S.C., 2022. Not biomass burning but stratospheric intrusion dominating tropospheric ozone over the Tibetan Plateau. *Proceedings of the National Academy of Sciences of the United States of America*, 119(38), e2211002119, DOI: 10.1073/pnas.2211002119.

Yin D.Y., Zhao S.P., Qu J.J., Yu Y., Kang S.C., Ren X.L., Zhang J., Zou Y., Dong L.X., Li J., He J.J., Li P., Qin D.H., 2020. The vertical profiles of carbonaceous aerosols and key influencing factors during wintertime over western Sichuan Basin, China. *Atmospheric Environment*, 223, 117269, DOI: 10.1016/j.atmosenv.2020.117269.

Yin X.F., Rupakheti D., Zhang G.S., Luo J.L., Kang S.C., de Foy B., Yang J.H., Ji Z.M., Cong Z.Y., Rupakheti M., Li P., Hu Y.L., Zhang Q.G., 2024. Surface ozone over the Tibetan Plateau controlled by stratospheric intrusion. *Atmospheric Chemistry and Physics*, 23(17), 10137–10143, DOI: 10.5194/acp-23-10137-2023.

Zhang L., Zhang H.S., Li Q.H., Cai X.H., Song Y., 2022. Vertical dispersion mechanism of long-range transported dust in Beijing: Effects of atmospheric turbulence. Atmospheric Research, 269, 106033, DOI: 10.1016/j.atmosres.2022.106033.

Zhang L., Zhang H.S., Cai X.H., Song Y., Zhang X.Y., 2024. Characteristics of turbulence intermittency, fine structure, and flux correction in the Taklimakan Desert. *Journal of the Atmospheric Sciences*, 81(2), 459–475, DOI: 10.1175/JAS-D-23-0107.1.

Zhang Y., Zhao T.L., Ning G.C., Xu X.D., Chen Z., Jia M., Sun X., Shu Z., Lu Z., Liu J., Qie X.S., 2025. A unique mechanism of ozone surges jointly triggered by deep stratospheric intrusions and the Tibetan Plateau topographic forcing. Geophysical Research Letters, 52(10), e2024GL114207, DOI: 10.1029/2024GL114207.

https://doi.org/10.5194/egusphere-2025-3130
Preprint. Discussion started: 28 July 2025

Zhao C.F., Yang Y.K., Fan H., Huang J.P., Fu Y.F., Zhang X.Y., Kang S.C., Cong Z.Y., Letu H., Menenti M., 2020. Aerosol characteristics and impacts on weather and climate over the Tibetan Plateau. *National Science Review*, 7(3), 492–495, DOI: 10.1093/nsr/nwz184.

Zhao S.P., Yu Y., Yin D.Y., Qin D.H., Yu Z.S., Dong L.X., Yang J.C., Mao Z.L., He J.J., Li P., 2019a. PM_1 carbonaceous aerosols during winter in a typical valley city of western China: Vertical profiles and the key influencing factors. *Atmospheric Environment*, 202, 75–92, DOI: 10.1016/j.atmosenv.2019.01.030.

Zhao S.P., Yu Y., Li J.L., Yin D.Y., Qi S.F., Qin D.H., 2021. Response of particle number concentrations to the clean air action plan: lessons from the first long-term aerosol measurements in a typical urban valley in western China. *Atmospheric Chemistry and Physics*, 21, 14959–14981, DOI: 10.5194/acp-21-14959-2021.

Zhao S.P., Qi S.F., Yu Y., Kang S.C., Dong L.X., Chen J.B., Yin D.Y., 2022. Measurement report: Contrasting elevation-dependent light absorption by black and brown carbon: lessons from in situ measurements from the highly polluted Sichuan Basin to the pristine Tibetan Plateau. *Atmospheric Chemistry and Physics*, 22(22), 14693–14708, DOI: 10.5194/acp-22-14693-2022.

Zhao S.P., He J.J., Dong L.X., Qi S.F., Yin D.Y., Chen J.B., Yu Y., 2023. Contrasting vertical circulation between severe and light air pollution inside a deep basin: Results from the collaborative experiment of 3D boundary-layer meteorology and pollution at the Sichuan Basin (BLMP-SCB). *Bulletin of the American Meteorological Society*, 104(2), E411–E434, DOI: 10.1175/BAMS-D-22-0150.1.

Zhao S.Y., Feng T., Tie X.X., Wang Z.B., 2020. The warming Tibetan Plateau improves winter air quality in the Sichuan Basin, China. *Atmospheric Chemistry and Physics*, 20(23), 14873–14887, DOI: 10.5194/acp-20-14873-2020.

Zhou C.L., Liu Y.Z., Zhu Q.Z., He Q., Zhao T.L., Yang F., Huo W., Yang X.H., Mamtimin A., 2022. In situ observation of warm atmospheric layer and the heat contribution of suspended dust over the Tarim Basin. *Atmospheric Chemistry and Physics*, 22(8), 5195–5207, DOI10.5194/acp-22-5195-2022.